A&A, 691, A359 (2024)
https://doi.org/10.1051/0004-6361/202449477

Astronomy & Astrophysics

Observational studies of S-bearing molecules in massive star-forming regions

R. Luo[1], J. Z. Wang[1,⋆], X. Zhang[2], D. H. Quan[3], X. J. Jiang[3], J. Li[4], Q. Gou[5], Y. Q. Li[4], Y. N. Xu[1], S. Q. Zheng[4], C. Ou[1], and Y. J. Liu[6]

[1] Guangxi Key Laboratory for Relativistic Astrophysics, School of Physical Science and Technology, Guangxi University, Nanning 530004, PR China
[2] Xinjiang Astronomical Observatory, Chinese Academy of Sciences, 150 Science 1-Street, Urumqi, Xinjiang 830011, PR China
[3] Research Center for Astronomical Computing, Zhejiang Laboratory, Hangzhou 311121, PR China
[4] Shanghai Astronomical Observatory, Chinese Academy of Sciences No. 80 Nandan Road Shanghai 200030, PR China
[5] School of Chemistry and Chemical Engineering, Chongqing University, Daxuecheng South Road. 55, Chongqing 401331, PR China
[6] Department of Physics, Anhui Normal University, Wuhu, Anhui 241002, PR China

Received 3 February 2024 / Accepted 14 October 2024

ABSTRACT

Context. S-bearing molecules are powerful tools for determining the physical conditions inside a massive star-forming region. The abundances of S-bearing molecules, including H_2S, H_2CS, and HCS^+, are highly dependent on physical and chemical changes, which means that they are good tracers of the evolutionary stage of massive star formation.

Aims. We present observational results of H_2S 1_{10}-1_{01}, $H_2{}^{34}S$ 1_{10}-1_{01}, H_2CS 5_{14}-4_{14}, HCS^+ 4-3, SiO 4-3, HC_3N 19-18, and $C^{18}O$ 1-0 toward a sample of 51 late-stage massive star-forming regions, and study the relationships between H_2S, H_2CS, HCS^+, and SiO in hot cores. We discuss the chemical connections of these S-bearing molecules based on the relations between the relative abundances in our sources.

Methods. $H_2{}^{34}S$ 1_{10}-1_{01}, as the isotopic line of H_2S 1_{10}-1_{01}, was used to correct the optical depths of H_2S 1_{10}-1_{01}. Beam-averaged column densities of all molecules were calculated, as were the abundances of H_2S, H_2CS, and HCS^+ relative to H_2, which were derived from $C^{18}O$. Results from a chemical model that included gas, dust grain surface, and icy mantle phases, were compared with the observed abundances of H_2S, H_2CS, and HCS^+ molecules.

Results. H_2S 1_{10}-1_{01}, $H_2{}^{34}S$ 1_{10}-1_{01}, H_2CS 5_{14}-4_{14}, HCS^+ 4-3, and HC_3N 19-18 were detected in 50 of the 51 sources, SiO 4-3 was detected in 46 sources, and $C^{18}O$ 1-0 was detected in all sources. The Pearson correlation coefficients between H_2CS and HCS^+ normalized by H_2 and H_2S are 0.94 and 0.87, respectively, and a tight linear relationship with a slope of 1.00 and 1.09 is found; this relationship is 0.77 and 0.98 between H_2S and H_2CS and 0.76 and 0.97 between H_2S and HCS^+. The full widths at half maxima of $H_2{}^{34}S$ 1_{10}-1_{01}, H_2CS 5_{14}-4_{14}, HCS^+ 4-3, and HC_3N 19-18 in each source are similar to each other, which indicates that they may trace similar regions. By comparing the observed abundance with model results, we see that there is one possible time ($2–3 \times 10^5$ yr) a which each source in the model matches the measured abundances of H_2S, H_2CS, and HCS^+. The abundances of HCS^+, H_2CS, and H_2S increase with the SiO abundance in these sources, which implies that shock chemistry may be playing a large role.

Conclusions. The close abundance relation of H_2S, H_2CS, and HCS^+ and the similar line widths in observational results indicate that these three molecules could be chemically linked, with HCS^+ and H_2CS the most correlated. The comparison of the observational results with chemical models shows that the abundances can be reproduced for almost all the sources at a specific time. The observational results, including the abundances in these sources need to be considered in further modeling of H_2S, H_2CS, and HCS^+ in hot cores with shock chemistry.

Key words. ISM: abundances – ISM: clouds – ISM: molecules

1. Introduction

As the tenth most abundant element in the Universe, with a relative abundance to hydrogen of $\sim 1.3 \times 10^{-5}$ (Asplund et al. 2005), sulfur (S) has been found in many molecules, which is important for understanding gas chemistry in molecular clouds with different phases. More than a dozen S-bearing molecules have been detected in interstellar molecular clouds and/or outflows, including SH, SH^+, SO, SO_2, CS, C_2S, C_3S, CH_3SH, NS, SiS, H_2S, H_2CS, HCS^+, OCS, HNCS, and HSCN (Gottlieb et al. 1978; Frerking et al. 1979; Brown et al. 1980; Blake et al. 1987; Drdla et al. 1989; Turner 1989; Adande et al. 2010; Esplugues et al. 2013; Neufeld et al. 2015; Li et al. 2015; Luo et al. 2019; Cernicharo et al. 2000). Though the S abundance in a diffuse HI medium is consistent with the cosmic value (Jenkins 2009), the main reservoir of S in dense clouds and hot core remains unclear (Vidal & Wakelam 2018) since the derived abundance of dense clouds only accounts for ∼0.01 of the cosmic abundance of atomic S (Charnley 1997).

S-bearing molecules are useful tracers of the chemical and physical properties of complex star-forming regions (SFRs) located in dense molecular clouds and can be used to study the evolutionary stages of massive star formation (Esplugues et al. 2014). Esplugues et al. (2013) showed that S-bearing molecules exhibit higher column densities, by up to three orders of magnitude, in the high-velocity plateau of Orion KL affected by shocks with respect to quiet regions of the clouds. Therefore, they are also considered to be good tracers of shocks. S-bearing

⋆ Corresponding author; junzhiwang@gxu.edu.cn

molecules released from ice mantles at T ∼ 100–300 K, such as SO, H_2S, H_2CS, and OCS, can probe hot cores in low-mass protostellar Class 0 systems (Tychoniec et al. 2021). Based on a sample of massive SFRs, Fontani et al. (2023) find that NS, CCS, and HCS^+ trace cold, quiescent, and likely extended material, OCS and SO_2 trace warmer, more turbulent, and likely denser and more compact material, and SO traces both quiescent and turbulent material. However, the chemical origin of H_2S and H_2CS is less clear.

Sulfur and oxygen are part of the chalcogens group in the periodic table and have similar electronic structure and chemical bonds, meaning that they usually have a similar reactivity in chemical reactions (Miessler et al. 2013). Oxygen, the third most abundant element after hydrogen and helium in the interstellar medium (ISM), has a cosmic abundance of O/H ∼ 2.5×10^{-4} (Lis et al. 2023). H_2O, H_2CO, and HCO^+, listed in order of decreasing abundances in the ISM, are important oxygen-containing molecules and have close astrochemical relationships. Oxygen being replaced with S, H_2S, H_2CS, and HCS^+ molecules – which may have relatively high abundances compared to other S-bearing molecules – likely plays an important role in the chemical network of S-bearing molecules in the ISM. For example, the abundances of H_2S, H_2CS, and HCS^+ molecules normalized by H_2 are 4.6×10^{-8}, 1.3×10^{-9}, and 1.5×10^{-10}, respectively, in G328.2551-0.5321 (Bouscasse et al. 2022).

There are few observational studies of H_2S, H_2CS, and HCS^+ molecules toward hot cores (Esplugues et al. 2013; Li et al. 2015; Kalenskii et al. 2022; el Akel et al. 2022; Esplugues et al. 2023). The dominant S-bearing species in ices are still a matter of debate. H_2S has been suggested since it is predicted to be to abundant on grain surfaces in low-gas, dust-temperature environments (Vidal et al. 2017; Navarro-Almaida et al. 2020, <20 K), but it has not been detected on ices (McClure et al. 2023). Once H_2S molecules form, they rapidly initiate reactions that drive the production of other S-bearing molecules (Druard & Wakelam 2012). The formation of S-bearing molecules is closely related to the environment, namely the temperature (Druard & Wakelam 2012), the presence of UV photons and high-energy protons (Jiménez-Escobar & Muñoz Caro 2011), and ion irradiation (Garozzo et al. 2010). In molecular clouds, ion-molecule reactions are most common (Goldsmith & Linke 1980), while in the warm gases of hot cores and shock waves, neutral-neutral reactions are most common (Charnley 1997). H_2CS may be formed by CH + H_2S in the gas phase of massive SFRs such as Orion KL and Sgr B2, as predicted by an astrochemical model (Inostroza-Pino et al. 2020). What's more, H_2CS can be formed via S + CH_3 and destroyed by C^+ in the gas phase (Esplugues et al. 2022). Finally, HCS^+ can be formed by CS + H_3^+ and CS^+ + H_2 in high-mass star-forming cores. (Shingledecker et al. 2020; Fontani et al. 2023) The dissociative recombination rate of HCS^+ is substantially higher than those of other isoelectronic ions, which has a substantial effect on the abundances of molecules and ions in the low-temperature environment of interstellar clouds (Montaigne et al. 2005). However, there is still a lack of sufficient studies on H_2S, H_2CS, and HCS^+ detections and the relationship among the three molecules in massive SFRs.

In this paper we present H_2S 1_{10}-1_{01}, $H_2{}^{34}S$ 1_{10}-1_{01}, H_2CS 5_{14}-4_{14}, HCS^+ 4-3, SiO 4-3, HC_3N 19-18, and $C^{18}O$ 1-0 single pointing observations toward a sample of 51 massive SFRs obtained with the Institut de Radioastronomie Millimétrique (IRAM) 30 m telescope. The observations are described in Section 2, and the results in Section 3. A discussion is presented in Section 4 and a brief summary in Section 5.

2. Observations and analysis

2.1. Observations and data reduction

The sample, which was selected from Reid et al. (2014, 2019), with measurements of trigonometric parallaxes, comprises 51 late-stage massive SFRs with 6.7 GHz methanol masers. The observations were taken with the IRAM 30 m telescope on Pico Veleta (Spain) in June and October 2016, August 2017, and August 2020. The 3 mm (E0) and 2 mm (E1) bands of the Eight Mixer Receiver (EMIR) were used simultaneously with the Fourier transform spectrometers backend to cover a 8 × 4 GHz bandwidth with 195 kHz spectral resolution for each band with dual polarization. More information can be found in Li et al. (2022). The spectral lines H_2S 1_{10}-1_{01} at 168 762.7623 MHz, $H_2{}^{34}S$ 1_{10}-1_{01} at 167 910.516 MHz, H_2CS 5_{14}-4_{14} at 169 114.160 MHz, HCS^+ 4-3 at 170 691.603 MHz, HC_3N 19-18 at 172 849.287 MHz, SiO 4-3 at 173 688.274 MHz, and $C^{18}O$ 1-0 at 109 782.1734MHz were included in the observations and used in our scientific analyses. Table 1 shows the source names, aliases, equatorial coordinates, and galactocentric distance. The spectroscopic parameters of the H_2S, $H_2{}^{34}S$, H_2CS, HCS^+, SiO, HC_3N, and $C^{18}O$ lines are given in Table 2.

The beam size of the IRAM 30 m telescope is 22.4″ at 110 GHz and 14.3″ at 172 GHz. The main beam brightness temperature (T_{mb}) was obtained as $T_{mb} = T_A^* \cdot F_{eff}/B_{eff}$, where T_A^* is the antenna temperature, F_{eff} the forward efficiency, and B_{eff} the main beam efficiency. F_{eff} and B_{eff} are 94 and 78% in the 3 mm band at 110 GHz, respectively, and 93 and 73% in the 2 mm band at 173 GHz.

The data were proceeded with CLASS package of the GILDAS software[1]. After averaging the spectra for each source to one single spectrum each in the 2 and 3 mm bands, the lines were identified and the first-order baseline was removed. The velocity-integrated flux, peak intensity, and central velocity of each line were derived for most of the lines via single-component Gaussian fitting. Otherwise, the "print area" in CLASS was used to derive the velocity-integrated flux if the line profile could not be well fitted via single-component Gaussian fitting (see Figure 1), due to self-absorption and/or multiple components (see Figures 1b and 1c) for lines above the 3σ level, while $H_2{}^{34}S$ 1_{10}-1_{01} was used to determine the velocity range of each source.

2.2. Methods

An optically thin transition produces an antenna temperature that is proportional to the column density in the upper level of the transition being observed (Goldsmith & Langer 1999). However, since sulfur is the tenth most abundant element in the Universe and H_2S is likely the dominant molecular form of the S element in molecular clouds, H_2S lines are usually optically thick. Some H_2S 1_{10}-1_{01} lines show a pit around the line center on the spectrum level, a signature of self-absorption. Since $H_2{}^{34}S$ 1_{10}-1_{01} lines are also detected with H_2S 1_{10}-1_{01}, we used the beam-averaged column densities of $H_2{}^{34}S$ to calculate those of H_2S using the $^{32}S/^{34}S$ ratio as a function of galactocentric distance Yan et al. (2023):

$$^{32}S/^{34}S = (0.75 \pm 0.13)R_{GC} + (15.52 \pm 0.78) \quad (1)$$

[1] http://www.iram.fr/IRAMFR/GILDAS

Table 1. Information on the sources and detected lines.

Source name Alias	RA(J2000) (hh : mm : ss)	Dec(J2000) (dd : mm : ss)	D_{GC} (kpc)	Line	$\int T_{mb}dv$ (K km s^{-1})	v_{LSR} (km s^{-1})	T_{peak} (K)
G121.29+00.65	00:36:47.35	63:29:02.2	8.8	HC_3N (19-18)	1.92 ± 0.03	−17.4 ± 0.1	0.69
L1287				^{a}H_2S (1_{10}-1_{01})	9.08 ± 0.04	−17.7 ± 0.1	2.03
				$H_2{}^{34}S$ (1_{10}-1_{01})	0.69 ± 0.03	−17.5 ± 0.1	0.24
				^{a}H_2CS (5_{14}-4_{14})	2.27 ± 0.02	−17.4 ± 0.1	0.81
				HCS^+ (4-3)	0.93 ± 0.02	−17.5 ± 0.1	0.37
				^{a}$C^{18}O$ (1-0)	7.06 ± 0.02	−17.6 ± 0.1	2.51
				SiO (4-3)	1.68 ± 0.06	−17.1 ± 0.1	0.42
G123.06-06.30	00:52:24.70	56:33:50.5	10.1	HC_3N (19-18)	2.77 ± 0.03	−30.8 ± 0.1	0.81
NGC281				H_2S (1_{10}-1_{01})	10.40 ± 0.03	−31.0 ± 0.1	2.07
				$H_2{}^{34}S$ (1_{10}-1_{01})	0.95 ± 0.02	−30.5 ± 0.1	0.26
				H_2CS (5_{14}-4_{14})	4.70 ± 0.02	−30.4 ± 0.1	1.24
				HCS^+ (4-3)	1.68 ± 0.03	−30.6 ± 0.1	0.46
				^{a}$C^{18}O$ (1-0)	5.87 ± 0.03	−30.0 ± 0.1	1.62
				SiO (4-3)	7.50 ± 0.08	−31.0 ± 0.1	0.42

Notes. Two methods were used to obtain $\int T_{mb}dv$: "print area" and Gaussian fitting. More information is available on Zenodo (https://doi.org/10.5281/zenodo.13937627).

Table 2. Spectroscopic information from the CDMS.

Line [a]	Frequency (MHz)	A_{ul} (s^{-1})	Q (T_{ex}=18.75K)	g_u	E_u (cm^{-1})	Ref. [b]
HC_3N 19-18	172849.300	4.08×10^{-4}	86.2	39	27.88	(Kalenskii et al. 2002)
$H_2{}^{34}S$ 1_{10}-1_{01}	167910.516	2.64×10^{-5}	8.72	9	27.83	(Minh et al. 1991)
H_2CS 5_{14}-4_{14}	169114.160	6.68×10^{-5}	91.2	33	37.54	(Thaddeus et al. 1972)
HCS^+ 4-3	170691.603	9.86×10^{-5}	18.7	9	20.48	(Gudeman et al. 1981)
SiO 4-3	173688.274	2.61×10^{-4}	18.3	9	20.84	(Schwartz et al. 1982)
$C^{18}O$ 1-0	109782.173	6.27×10^{-8}	7.46	3	5.27	(Ulich & Haas 1976)

Notes. [a]All parameters are taken from the CDMS catalog. [b]Reference paper where the observations are presented.

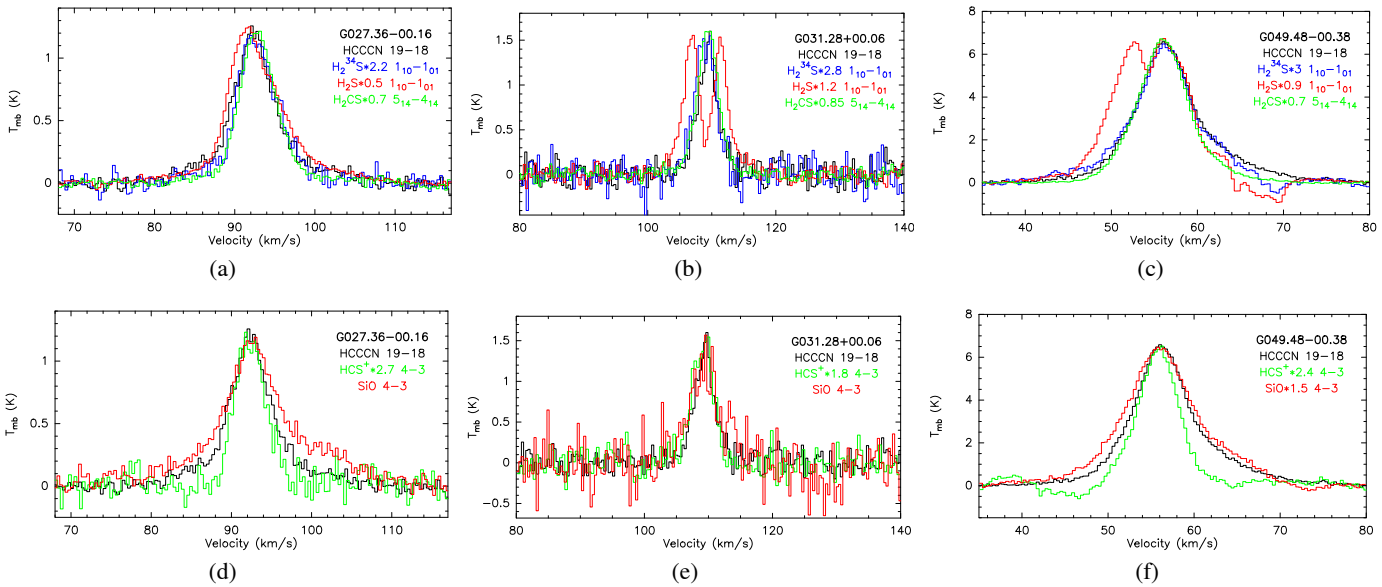

Fig. 1. Spectra of H_2S 1_{10}-1_{01}, $H_2{}^{34}S$ 1_{10}-1_{01}, and H_2CS 5_{14}-4_{14} detected with IRAM for three sources (a, b and c) and HCS^+ 4-3 and SiO 4-3 lines (d, e and f). All of the observed spectra are aligned to the peak of HC_3N 19-18. In panels (a), (b), and (c), red lines are H_2S 1_{10}-1_{01}, blue lines are $H_2{}^{34}S$ 1_{10}-1_{01}, and green lines are H_2CS 5_{14}-4_{14}. In (d), (e), and (f), HCS^+ 4-3 lines are in green and SiO 4-3 lines are red. The black lines in all panels represent HC_3N.

The beam-averaged column density is

$$N_{tot} = \frac{8\pi k\nu^2}{hc^3 A_{ul}} \frac{Q(T_{ex})}{g_u} e^{\frac{E_u}{kT_{ex}}} \int T_{mb}\, \mathrm{d}v \qquad (\mathrm{cm}^{-2}) \tag{2}$$

Here, k is the Boltzmann constant, ν the transition frequency, h the Planck constant, c the speed of light, A_{ul} the Einstein emission coefficient, g_u the upper state degeneracy and E_u the upper state energy. For undetected sources, 3σ upper limits for the integrated intensity, $\int T_{mb}\, \mathrm{d}v$, were calculated as $3 \times \mathrm{rms} \sqrt{\delta v \Delta v}$, where: δv is the channel separation in velocity; rms is the root mean square for the line-free channel determined first-order linear fitting using the remaining channels, which are masked in the signal area; and Δv is the line width.

With the following assumptions, we calculated beam-averaged column densities: (i) a unity beam filling factor; (ii) a local thermodynamic equilibrium (LTE) approximation for all molecules with the same excitation temperature (T_{ex}) of 18.75 K for $H_2{}^{34}S$, H_2CS, HCS^+, SiO, and $C^{18}O$; and (iii) the lines of all these molecules are optically thin. Since the $H_2{}^{34}S$, H_2CS, and HCS^+ molecules are normally sub-thermal in these sources, the T_{ex} used for these spectral lines are lower than the kinetic temperature (T_k). The partition function ($Q(T_{ex})$) for each molecule was obtained at T_{ex}=18.75 K, and this was verified using RADEX on the line calculator (van der Tak et al. 2007). For example, the upper level populations of $H_2{}^{34}S$ 1_{10}-1_{01} across all energy levels (POP-UP) were obtained using RADEX. When T_k ranges from 30 to 150 K and the density of H_2 is 1×10^5 cm^{-3}, POP-UP increases from 0.163 to 0.267. The values of $Q(T_{ex})$ were taken from Cologne Database for Molecular Spectroscopy[2] (Müller et al. 2001, 2005). Under an LTE approximation with T_{ex} = 18.75 K, $g_u e^{\frac{-E_u}{kT_{ex}}}/Q(T_{ex})$ – which is the same parameter as POP-UP in the RADEX results when calculating the total column density – is 0.234. We also calculated the systemic bias of estimating column densities with excitation temperatures of 37.5 (0.177), 25 (0.222), and 10 K (0.150), which is respectively about 1.32, 1.05, and 1.55 times of that with T_{ex} = 18.75 K for $H_2{}^{34}S$ molecules. The column densities of H_2 can be derived from $C^{18}O$ using the equation $N_{H_2} = 4.37 \times 10^6 N_{C^{18}O}$ (Frerking et al. 1982).

There is an alternate to using $H_2{}^{34}S$ column densities with the $^{32}S/^{34}S$ ratio to directly calculate the column density of H_2S: correcting the optical depths of H_2S. We assumed the H_2S and $H_2{}^{34}S$ 1_{10}-1_{01} lines in each source have the same excitation temperature (T_{ex}) and that the molecular abundance ratio is approximately equal to the isotopic abundance ratio (i.e., $\frac{^{32}S}{^{34}S} = \frac{H_2{}^{32}S}{H_2{}^{34}S}$; hereafter H_2S for $H_2{}^{32}S$). The τ_{H_2S} was then calculated as

$$\frac{1 - e^{-\tau_{H_2S}}}{1 - e^{-\tau_{H_2{}^{34}S}}} = \frac{\int T_{mb}(H_2S)\, \mathrm{d}v}{\int T_{mb}(H_2{}^{34}S)\, \mathrm{d}v}. \tag{3}$$

The calculated τ_{H_2S} ranges from 0.53 in G232.62+00.99 to 11.2 in G010.47+00.02 (see Table A.1). The column density calculation formula is slightly different from that of Eq. (1):

$$N_{tot} = \frac{8\pi k\nu^2}{hc^3 A_{ul}} \frac{Q(T_{ex})}{g_u} e^{\frac{E_u}{kT_{ex}}} \frac{\tau}{1 - e^{-\tau}} \int T_{mb}\, \mathrm{d}v \qquad (\mathrm{cm}^{-2}) \tag{4}$$

Comparing the column densities obtained via the two methods, we find that the column densities calculated directly from $H_2{}^{34}S$ using the $^{32}S/^{34}S$ ratio were 0.85 times lower than those calculated from the optical depth of the H_2S transition (see Table B.1).

[2] https://cdms.astro.uni-koeln.de/classic/predictions/catalog/partition_function.html

3. Results

3.1. The detected lines

Lines of H_2S 1_{10}-1_{01}, $H_2{}^{34}S$ 1_{10}-1_{01}, H_2CS 5_{14}-4_{14}, HCS^+ 4-3, and HC_3N 19-18 were detected in all sources except for G012.90-00.24, SiO 4-3 was detected in 46 sources, and $C^{18}O$ 1-0 was detected in all sources (see Figures 1 and A.1). The H_2S 1_{10}-1_{01} lines are generally stronger than H_2CS 5_{14}-4_{14}, while H_2CS 5_{14}-4_{14} lines are stronger than HCS^+ 4-3. The sources can be divided into three groups based in the line profile of H_2S 1_{10}-1_{01} and $H_2{}^{34}S$ 1_{10}-1_{01}. For 26 sources of the sample, including G027.36-00.16 (see Figure 1a), both lines can be fitted with a single Gaussian component, while in 21 sources, including G031.28+00.06 (see Figure 1b), H_2S 1_{10}-1_{01} needs from two to four components, and this is probably caused by inflowing gas. There are three sources, G049.48-00.38 (W51M, see Figure 1c), G043.16+00.01 (W49N), and G000.67-00.03 (SgrB2), in which there is a possible optically thin velocity component of H_2S 1_{10}-1_{01} that does not correspond to $H_2{}^{34}S$ 1_{10}-1_{01} emission. The column densities of H_2S were calculated from those of $H_2{}^{34}S$ for all the sources.

We used HC_3N 19-18 to confirm the central velocities and line profile of S-bearing lines, and $C^{18}O$ to obtain H_2 column densities and thereby the relative H_2S, H_2CS, and HCS^+ abundances. SiO was used as the tracer of shock activities in SFRs.

Table 1 shows the molecular species, velocity-integrated intensities, central velocity, and peak temperature. Velocity-integrated fluxes were obtained from the single-component Gaussian fitting, or with the "print area" for H_2S, H_2CS, and $C^{18}O$ in CLASS if a complex line profile was found (see Section 2.2; there instances are noted with an "a" superscript in column 4 of Table 1). As shown in Table 1, the velocity-integrated intensities and peak temperature of H_2S 1_{10}-1_{01} are higher than those of H_2CS 5_{14}-4_{14}, while those of H_2CS 5_{14}-4_{14} are higher than those of HCS^+ 4-3. The S-bearing species studied in this work have similar line widths, while SiO 4-3 has a broader line width than the other lines in each source.

3.2. Column densities

The beam-averaged column densities of H_2S, $H_2{}^{34}S$, H_2CS, HCS^+, SiO, and $C^{18}O$ molecules are shown in Table B.1. The H_2S ranges from 3.59×10^{13} to 3.50×10^{15}cm^{-2}, $H_2{}^{34}S$ from 1.65×10^{12} to 1.83×10^{14}cm^{-2}, H_2CS from 7.09×10^{12} to 1.25×10^{15}cm^{-2}, and HCS^+ from 6.67×10^{11} to 6.04×10^{13}cm^{-2}. HCS^+ is the lowest abundant molecules among H_2S, H_2CS and HCS^+. The resulting column densities for SiO and $C^{18}O$ molecules in these 50 sources range from 3.33×10^{11} to 9.25×10^{13}cm^{-2} and from 6.30×10^{15} to 3.76×10^{16}cm^{-2}, respectively. The column densities of H_2 were derived from $C^{18}O$ as $N_{H_2} = 4.37 \times 10^6 N_{C^{18}O}$ (Frerking et al. 1982) and range from 1.13×10^{22} to 4.80×10^{23}cm^{-2}.

3.3. Relative abundances

The relative abundances of these molecules, which can be obtained with beam-averaged column densities, are more important than the beam-averaged column densities themselves for scientific analyses. The abundances of H_2S, H_2CS, and HCS^+ normalized by H_2 are shown in Table D.1; the H_2S abundances were obtained by multiplying $H_2{}^{34}S$ abundance by the $^{32}S/^{34}S$ ratios. The relation between the abundances of H_2S and HCS^+

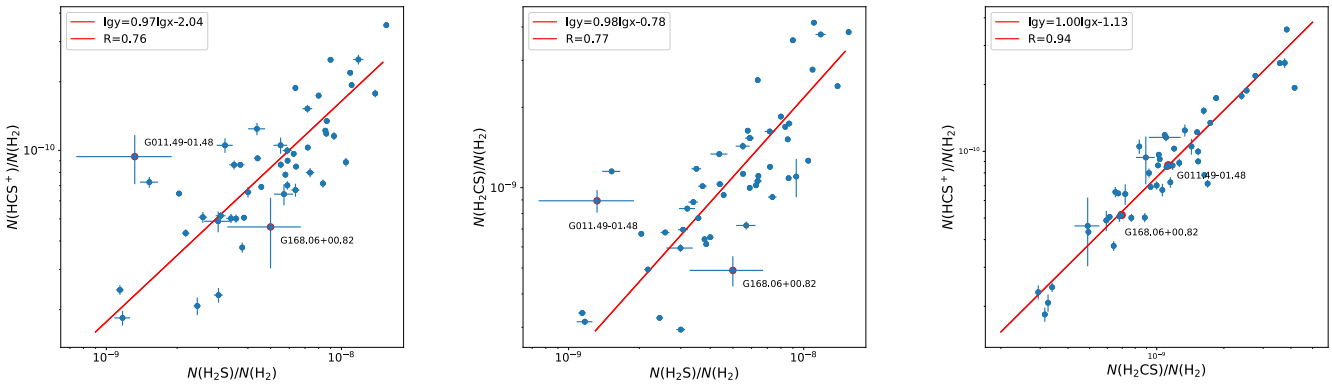

(a) (b) (c)

Fig. 2. Relationship between the HCS^+ and H_2S abundances (a), H_2CS and H_2S abundances (b), and HCS^+ and H_2CS abundances (c), all normalized by H_2. The fitting lines, generated using the least square method, are marked in red. G011.49-01.48 and G0168.06+00.82, which have large errors, are marked where $H_2{}^{34}S$ lines show weak emission.

normalized by H_2 and determined via least square fitting is presented in Figure 2a; it has a Pearson correlation coefficient[3] of 0.76 and a slope of 0.97. Also shown are the abundances of H_2S and H_2CS normalized by H_2 with a Pearson correlation coefficients and slope of 0.77 and 0.98, respectively (see Figure 2b). For the abundances of H_2CS and HCS^+ normalized by H_2 (see Figure 2c), the Pearson correlation coefficients and slope were 0.94 and 1.00. Since the slopes and Pearson correlation coefficients are are positive numbers close to or equal to 1, H_2S, H_2CS, and HCS^+ molecules are probably very closely chemically related to each other.

The relative abundances of H_2S, H_2CS, and HCS^+ normalized by H_2 of these 50 sources span more than one order of magnitude. Table E.1 shows the abundance ratios [H_2S/H_2CS], [H_2S/HCS^+], and [H_2CS/HCS^+] toward all the sources. The abundance ratio of: [H_2S/H_2CS] ranges from 1.32±0.12 in G000.67-00.03 to 10.2 ± 0.49 in G109.87+02.11 with a median value of 4.4; [H_2S/HCS^+] from 14.1 ± 7.01 in G011.49-01.48 to 129.6 ± 11.1 in G109.87+02.11 with a median value of 63.8; and [H_2CS/HCS^+] from 7.94 ± 0.61 in G232.62+00.99 to 23.6 ± 0.96 in G049.48-00.36 with a median value of 13.0.

A good correlation is found between H_2CS and HCS^+ whether normalized by H_2S or H_2 (see Figures 3 and 2c). The abundance ratios of [H_2CS/HCS^+] are within a narrower range than that of [H_2S/HCS^+] and [H_2S/H_2CS] (see Table E.1). G011.49-01.48 and G0168.06+00.82 ,with large errors, are marked where $H_2{}^{34}S$ lines show weak emission in Figures 2 and 3.

The relationships between S-bearing molecules and SiO, normalized by H_2, are shown in Figure 4, with Pearson correlation coefficients of HCS^+, H_2CS, and H_2S with SiO of 0.60, 0.68, and 0.57, and slopes of 0.73, 0.75, and 0.72, respectively. Though the correlations are not as tight as that between the S-bearing molecules themselves (see Figure 2), the abundances of HCS^+, H_2CS, and H_2S increase with the SiO abundance in these sources. Shock chemistry might be needed in further modeling.

3.4. Line profiles

In most cases, the lines are very well fitted with a single Gaussian (see Figures 1 and A.1). This is especially apparent in $H_2{}^{34}S$, H_2CS, HCS^+, and HC_3N (except for H_2S and SiO). The full widths at half maxima (FWHMs) are similar to each other for the $H_2{}^{34}S$, H_2CS, HCS^+, and HC_3N lines in each source, between 1 km s^{-1} and 10 km s^{-1} (see Table C.1), except for G000.67-00.03 (Sgr B2) and G043.16+000.01 (W49N). Figure 5 shows a comparison of the FWHMs of the observed lines: the correlation between HCS^+ and H_2CS is perfect, with a Pearson correlation coefficient of 0.98; it is good between H_2CS and $H_2{}^{34}S$ (0.94), HCS^+ and $H_2{}^{34}S$ (0.95), and HCS^+ and HC_3N (0.92). Such results indicate that these observed $H_2{}^{34}S$, H_2CS, HCS^+, and HC_3N transitions trace the same gas.

[3] The Pearson correlation coefficient is a measure of the linear relationship between two variables. The closer |γ| is to 1, the stronger the linear relationship.

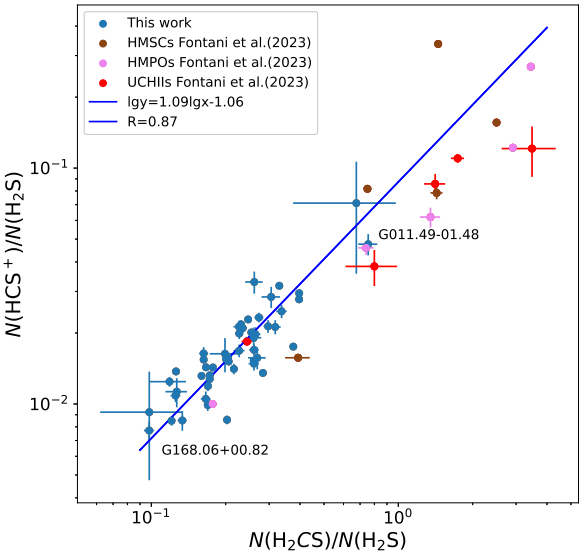

Fig. 3. Distribution of the H_2CS and HCS^+ molecular abundances in each source. Two sources (G011.49-01.48 and G0168.06+00.82) have large errors due to the weak emission of the $H_2{}^{34}S$ lines. The molecular abundance ratios from Fontani et al. (2023) are also presented.

4. Discussion

4.1. Possible chemical connections between H_2S, H_2CS, and HCS^+ in hot cores?

S-bearing species are good tracers of hot cores because they are particularly sensitive to physical and chemical changes in

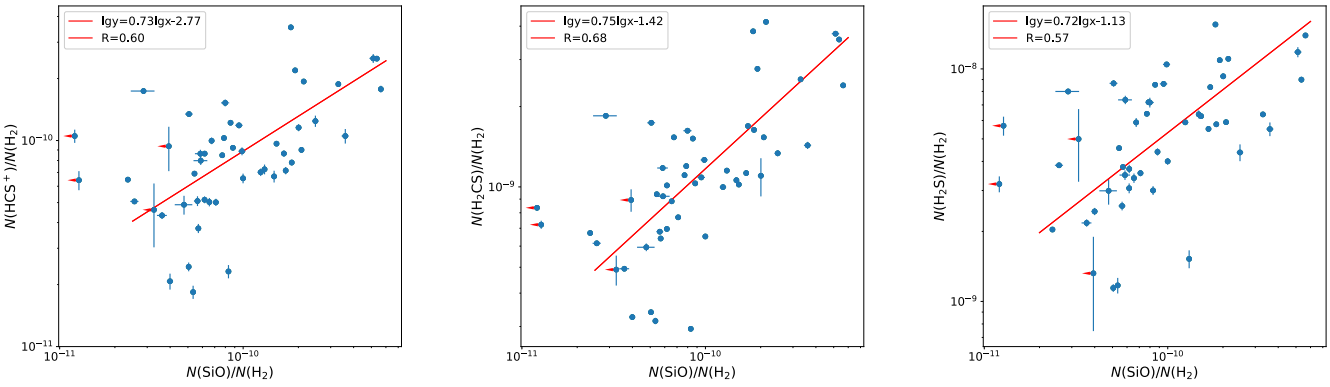

Fig. 4. Relationships between the HCS^+ and SiO abundances (a), H_2CS and SiO abundances (b), and H_2S and SiO abundances (c), all normalized by H_2. The fitting lines, generated using the least square method, are marked in red. The four points marked with red arrows are realistic upper limits of SiO and were not used in the fitting.

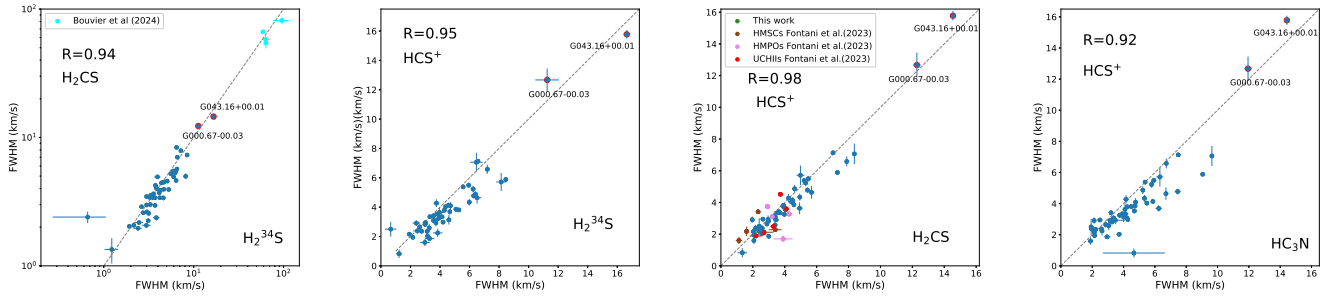

Fig. 5. Comparison of the line FWHMs of the observed species. In all plots, the two distant blue points with red circles represent G000.67-00.03 (Srg B2) and G043.16+00.01 (W49N). The number in the upper-left corner of each panel is the Pearson correlation coefficient, ρ. The gray line is y=x. The ratios from Bouvier et al. (2024) and Fontani et al. (2023) are also presented.

dense and hot regions (Hatchell et al. 1998). H_2S is the main molecular form of S-bearing molecules in molecular clouds, which may be produced on the surface of grains, and the rapid reactions of H_2S molecules can drive the production of other S-bearing molecules (Druard & Wakelam 2012). The measured abundances of H_2S:H_2CS:HCS^+ in these 50 sources show that H_2S is more abundant than H_2CS, and HCS^+, and H_2O is more abundant than H_2CO and HCO^+ (Herbst & Klemperer 1973).

With a correlation coefficient of 0.94, the correlation between the abundances of HCS^+ and H_2CS is tighter than the correlation between either of these two molecules and H_2S (see Figure 2c). This is likely due to different chemical formation processes for H_2S compared to HCS^+ and H_2CS in chemical models. H_2S is mainly formed on grain surfaces (Druard & Wakelam 2012), while the other two molecules are primarily formed in the gas phase (Vidal & Wakelam 2018; Gronowski & Kołos 2014). Additionally, the elemental carbon also affects the formation of H_2CS and HCS^+, which can reflect the better correlation of HCS^+ versus H_2CS than that of HCS^+ versus H_2S and H_2CS versus H_2S in observations. Not only the correlation coefficients, but also the slopes of the fitting results can be used to substantiate the relation between the abundances of the two molecules. We find a tight linear relationship between HCS^+ and H_2CS, with slope of 1.00; the relation between H_2CS and H_2S is 0.98, and it is 0.97 for HCS^+ and H_2S.

Our sample comprises 51 massive late-stage SFRs, while the sample in Fontani et al. (2023) comprises 15 sources at different stages (see Figure 3). The HCS^+/H_2S versus H_2CS/H_2S trend found in this work is also found in Fontani et al. (2023). We obtained line widths and excitation temperatures to confirm that HCS^+ preferentially traces quiescent and likely extended material. Our results show that the line widths of the $H_2{}^{34}S$, H_2CS, HCS^+, and HC_3N lines in each source are almost the same (see Figure 5), which indicates that they may be from the same gas.

4.2. Chemical model including gas, dust grain surface and icy mantle phases, for H_2S, H_2CS, and HCS^+

To better understand the observed abundances of H_2S, H_2CS, and HCS^+ in hot cores, we utilized the three-phase NAUTILUS chemical code (Ruaud et al. 2016), which takes the gas, dust grain surface, and icy mantle into consideration. We combined it with a similar physical model from Zhang et al. (2023), in which a collapse stage is followed by a warm-up stage. During the collapse stage, the gas density was initially set to 3×10^3 cm^{-3} and gradually increased to the final density of 1.6×10^7 cm^{-3} over a period of 1×10^6 years. The gas temperatures were fixed to 10 K during this stage. The density gradually increases over time, resulting in an increase in extinction, as shown in the left panel of Fig. 6. Once the peak density was achieved, the density was fixed and the gas and dust temperatures were raised from ~10 K to their peak temperatures in 2×10^5 years during the warm-up stages, as shown in the right panel of Fig. 6. The main physical parameters of hot core models are summarized in Table 3. For our simulations, we used initial abundances from Table 1 of Vidal & Wakelam (2018). The chemical network is based on the research of Vidal et al. (2017).

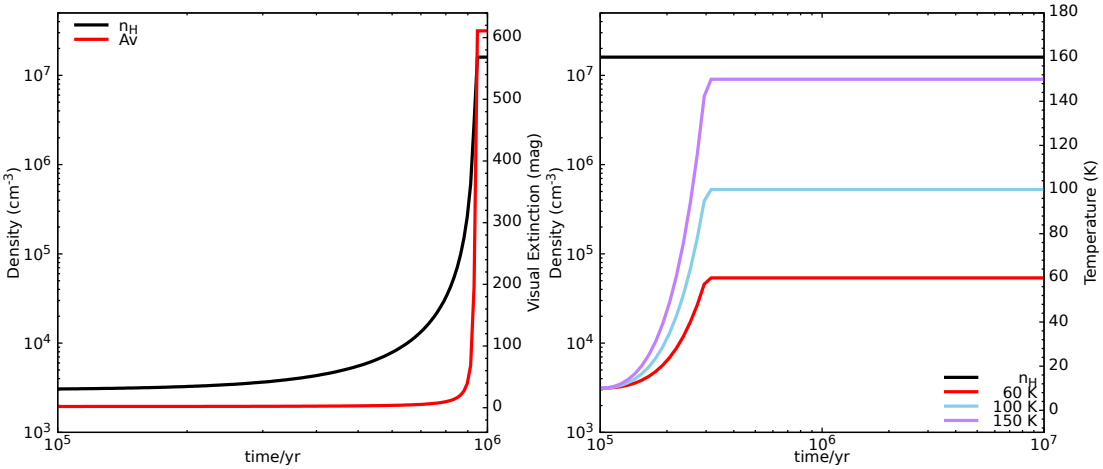

Fig. 6. Density, temperature, and A_V profiles as functions of time for collapse and warm-up stages in hot core models. Left: collapse stage. The gas density gradually increases from 3×10^3 cm^{-3} to 1.6×10^7 cm^{-3} over a period of 1×10^6 years, and the temperature remains at a constant value of 10 K. An increase in gas density leads to an increase in visual extinction. Right: warm-up stage. The gas density and visual extinction are 1.6×10^7 cm^{-3} and 6.109×10^2 mag, respectively; we used three values for T_{max}: 60, 100 and 150 K.

Table 3. Physical parameters of hot core models.

Source(Stage)	n_H (cm^{-3})	T (K)	A_V (mag)	ζ (s^{-1})	UV factor (Habing)
The free fall collapse [a,b]	$3 \times 10^3 \rightarrow 1.6 \times 10^7$	10	$2 \rightarrow 6.109 \times 10^2$	1.3×10^{-17}	1
The warm-up [b,c]	1.6×10^7	$10 \rightarrow 60, 100, 150$	6.109×10^2	1.3×10^{-17}	1

Notes. [a]Garrod & Herbst (2006), [b]Bonfand et al. (2019), [c]Coutens et al. (2018).

In the warm-up stage, H_2S is mainly formed through the following hydrogenation reactions on grain surfaces:

$$S + H \rightarrow HS + H \rightarrow H_2S. \quad (5)$$

Some H_2S is already released back into the gas phase through reactive desorption before the temperature rises. When the temperature reaches high values after 2×10^5 yr, it can return to the gas phase through a thermal process, which plays a dominant role in the production of gaseous H_2S. Initially, H_2S is mainly destroyed by H_3^+ via ion-neutral reactions in all cases. However, after 2×10^5 yr, 7×10^5 yr, and 3×10^5 yr, it is mainly destructed by atomic carbon for a T_{max} of 60 and 100 K and by atomic hydrogen for a T_{max} of 150 K in the gas phase, respectively. The related reactions are as follows:

$$H_2S + H_3^+ \rightarrow H_2 + H_3S^+; \quad C + H_2S \rightarrow HCS + H; \quad H + H_2S \rightarrow H_2 + HS. \quad (6)$$

H_2CS is primarily formed in the gas phase through the following neutral-neutral reaction:

$$S + CH_3 \rightarrow H_2CS + H. \quad (7)$$

and it follows a similar destruction pathway as H_2S, as both are initially broken down through the ion H_3^+. After 5×10^5 yr, 7×10^5 yr, and 9×10^5 yr in the gas phase, it is mainly destroyed by atomic carbon for T_{max} of 60, 100, and 150 K, respectively. The reactions proceed as follows:

$$H_2CS + H_3^+ \rightarrow H_2 + H_3CS^+; \quad H_2CS + C \rightarrow HC_2S + H. \quad (8)$$

Initially, HCS^+ is mainly formed through the reaction of CS with the H_3^+ ion in all cases. However, after 3×10^5 yr and 7×10^5 yr, it is primarily produced via the reactions $CS + HCO^+$ and $CS + HCNH^+$ for T_{max} of 60 and 150 K, respectively. The related reactions are as follows:

$$CS + H_3^+ \rightarrow HCS^+ + H_2; \quad CS + HCO^+ \rightarrow CO + HCS^+; \quad CS + HCNH^+ \rightarrow HCN + HCS^+. \quad (9)$$

It is mainly destroyed in the gas phase via the following electron recombination:

$$HCS^+ + e^- \rightarrow S + CH. \quad (10)$$

Both H_2S and H_2CS can be destroyed via reactions with H_3^+ (see Eqs. (6) and (8)). The main formation path of HCS^+ is a reaction with H_3^+ (see Eq. (9)). The relations of H_2S, H_2CS, and HCS^+ with H_3^+ can cause a close connection between them.

Like other similar O-bearing species, H_2CO could be produced from H_2O+CO, and is the second most abundant product after CO_2, at different concentrations of H_2O:CO mixtures (de Barros et al. 2022). Other processes can form H_2CO from H_2O, such as H_2O+C $\rightarrow$ H_2CO at temperatures associated with the ISM and in the cooler regions around young stars (Potapov et al. 2021). This shows that H_2CO is formed in a different way with H_2CS. The formation of HCO^+ under different A_v is different. From $A_v \sim 0.4$ to 3, the dominant reaction is $CO^+ + H_2$, while above 3, the dominant reaction is $H_3^+ + CO$ in molecular clouds (Panessa et al. 2023). HCO^+ can be destroyed by C_3H_2 (Narita et al. 2024). The formation paths of HCO^+ and HCS^+ seem to be the same in particular cases.

The model results of the relative abundances of H_2S, H_2CS, and HCS^+ species in the gas phase varying with time in warm-up stages are presented in Figure 7 with three different maximum

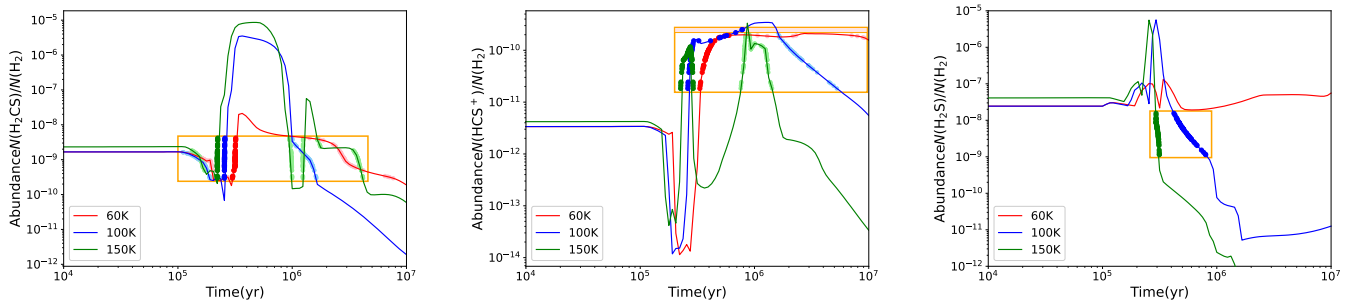

Fig. 7. Chemical model including the gas, the dust grain surface and the icy mantle. The solid lines correspond to the gas-phase abundances versus time during warm-up stages in chemical models with gas maximum temperatures of 60, 100, and 150 K, and the points are the observed data. The abundances of H_2CS, HCS^+ and H_2S relative to H_2 are presented in panels (a), (b), and (c), respectively. Since the samples are in the same evolutionary stage, two possible times from the form model are marked, with filled and transparent circles. Note that there are no intersections for H_2S at 60 K in model.

temperatures (T_{max}): 604, 100, and 150 K. The measured abundances are compared with the abundances from the model, which can have the same value at different times (see Figure 7). The samples are in the same evolutionary stage, and the more reasonable intersections are marked, as are other possible times. We considered the calculated abundance to be consistent with the observed value if the calculated abundance differs from the observed value by less than one order of magnitude.

For T_{max}=60 K (see Figure 7, red lines), the abundance of H_2S and H_2CS varies much less than that of HCS^+. Additionally, there is one possible time (3×10^5 yr) for each source that matchs the measured [H_2CS/H_2] and [HCS^+/H_2] abundances (see Figures 7a and 7b, red line and filled circles) and no intersection for [H_2S/H_2] (see Figure 7c). However, the discrepancy is less than one order of magnitude. The overprediction of H_2S that we find relative to the observational results could be a result of the absence of effective gas-phase destruction reactions in the H_2S chemistry within our model. [HCS^+/H_2] abundances in all sources range from 1.84×10^{-11} to 3.54×10^{-10}, and four of them rang from 2.19×10^{-10} to 3.54×10^{-10}, which is higher than the model results (see Figure 7b, orange filled rectangle). All sources with measured [H_2CS/H_2] abundances, which range from 2.94×10^{-10} to 4.15×10^{-9}, match the model results.

The abundances of H_2CS and HCS^+ change more quickly than H_2S, in 1×10^5 to 1×10^7 yr, with T_{max}=100 K (see Figure 7, blue lines). There is not a single time in common between the observed value and the model. The solutions are totally different for different molecules (see Figure 7), with about 2×10^5 yr for [H_2CS/H_2], 3×10^5 yr for [HCS^+/H_2], and 5×10^5 yr for [H_2S/H_2].

The possible times with T_{max}=150K for each source to match the measured abundances of [H_2S/H_2] are concentrated around 3×10^5 yr (see Figure 7c, green lines). Of the two to four possible time solutions for [H_2CS/H_2] and [HCS^+/H_2], the earliest is the most likely for most sources; one time is shared by the different abundances in each source, around 3×10^5 yr.

In general, the models can reproduce the observed abundances at around 2–3 $\times$ 10^5 yr for almost all of the sources. However, there is a small discrepancy for lower-T_{max} (60 K) models of H_2S. H_2CS and HCS^+ can be efficiently formed in the gas phase, while H_2S already chemically desorbs during its formation on the grains before being thermally desorbed. The abundance of H_2S cannot sharply increase like at the T_{max} of 100 and 150 K after the temperature reaches T_{max} of 60 K because it does not reach the desorption temperature of H_2S (around 70 K). In this condition, the chemical desorption is the primary origin for gaseous H_2S. Since gas-phase destruction reactions for H_2S are not as effective at the relatively low temperature of 60 K (compared to the T_{max} of 100 and 150 K), the abundance of H_2S is overpredicted in our model.

4.3. Shock activities

SiO is considered to be an excellent tracer of shock activities in SFRs because the SiO abundance in molecular outflows is at least three orders of magnitude higher than in quiescent gas (Schilke et al. 1997). Lots of elemental Si is probably in the form of stable materials in dust, like silicates, and is effectively trapped. Shock activities is needed to destroy silicates to release Si atoms from grains into the gas phase (Martin-Pintado et al. 1992), and the abundance of S-bearing molecules can be increased via moderate shocks (Wakelam et al. 2004).

SiO 4-3 was detected in 46 of the 51 sources in our sample (see the green lines in Figures 1 d–f), which indicates shock activities. The abundances of HCS^+, H_2CS, and H_2S increase with the SiO abundance in these sources (see Figure 4), which implies that shock chemistry is important for HCS^+, H_2CS, and H_2S. In addition, the line width of SiO is larger than those of the S-bearing species. This indicates that the SiO is actually tracing a different physical component with a different velocity broadening. SiO likely traces shocked regions, which implies that the S-bearing species are either tracing weaker shocks not traced by SiO or are actually tracing the hot core regions.

5. Summary and conclusions

We observed H_2S 1_{10}-1_{01}, $H_2{}^{34}S$ 1_{10}-1_{01}, H_2CS 5_{14}-4_{14}, HCS^+ 4-3, HC_3N 19-18, SiO 4-3, and $C^{18}O$ 1-0 toward a sample of 51 massive SFRs with the IRAM 30 m telescope. We derived beam average column densities, as well as their abundances with respect to H_2, from $C^{18}O$.

All lines can be well fitted with a single Gaussian, except for H_2S and SiO. The FWHMs are between 1 km s^{-1} and 10 km s^{-1} in all sources, except for G000.67-00.03 (Sgr B2) and G043.16+00.01 (W49N). The line FWHMs of the observed species are positively correlated with each other and have similar ranges, which indicates that they may trace similar regions.

The abundance ratios of [H_2S/H_2], [H_2CS/H_2], and [HCS^+/H_2] range by more than one magnitude with high correlation coefficients and positive slopes: a correlation coefficient of 0.94 and a slope of 1.00 for [H_2CS/H_2] and [HCS^+/H_2], and

0.76 and 0.97 for [H_2S/H_2] and [HCS^+/H_2]. For [H_2CS/H_2] and [H_2S/H_2] the correlation coefficients and slope are 0.77 and 0.98. These close relations indicate that these S-bearing molecules may have chemical connections with each other, with HCS^+ and H_2CS the most correlated based on the relations between the relative abundances of these molecules and those of the other 50 sources.

The three-phase NAUTILUS chemical code was utilized to simulate the relationship of three S-bearing molecules. Comparing the results of observation and model, we find one possible time ($2–3 \times 10^5$ yr) at which each source in the model matches the measured abundances of H_2S, H_2CS, and HCS^+. The abundances of HCS^+, H_2CS, and H_2S increase with the SiO abundance in these sources, which implies that shock chemistry may be important for them. Shock activity needs to be considered in further modeling of H_2S, H_2CS, and HCS^+ in hot cores.

Data availability

More information about H_2S 1_{10}-1_{01}, $H_2{}^{34}S$ 1_{10}-1_{01}, H_2CS 5_{14}-4_{14}, HCS^+ 4-3, HC_3N 19-18, SiO 4-3, and $C^{18}O$ 1-0 lines from our sample is available on Zenodo under the following link: https://doi.org/10.5281/zenodo.13937627

Acknowledgements. R.L., J.Z.W., Y.N.X., and C.O. are supported by National Key R&D Program of China (2023YFA1608204) and the National Natural Science Foundation of China grant 12173067. D.H.Q. and X.J.J. are supported by the National Natural Science Foundation of China (Grant No. 12373026), the Leading Innovation and Entrepreneurship Team of Zhejiang Province of China (Grant No. 2023R01008), and the Key R&D Program of Zhejiang, China (Grant No. 2024SSYS0012). This study is based on observations carried out under project number 012-16, 023-17 and 005-20 with the IRAM 30 m telescope. IRAM is supported by INSU/CNRS (France), MPG (Germany) and IGN (Spain).

References

Adande, G. R., Halfen, D. T., Ziurys, L. M., et al. 2010, ApJ, 725, 561
Asplund, M., Grevesse, N., & Sauval, A. J. 2005, ASP Conf. Ser., 336, 25
Blake, G. A., Sutton, E. C., Masson, C. R., et al. 1987, ApJ, 315, 621
Bonfand, M., Belloche, A., Garrod, R. T., et al. 2019, A&A, 628, A27
Bouscasse, L., Csengeri, T., Belloche, A., et al. 2022, A&A, 662, A32
Bouvier, M., Viti, S., Behrens, E., et al. 2024, A&A, 689, A64
Brown, R. D., Godfrey, P. D., & Winkler, D. A. 1980, MNRAS, 190, 1
Cernicharo, J., Guélin, M., & Kahane, C. 2000, A&AS, 142, 181
Charnley, S. B. 1997, ApJ, 481, 396
Chin, Y.-N., Henkel, C., Whiteoak, J. B., et al. 1996, A&A, 305, 960
Coutens, A., Willis, E. R., Garrod, R. T., et al. 2018, A&A, 612, A107
Drdla, K., Knapp, G. R., & van Dishoeck, E. F. 1989, ApJ, 345, 815
Druard, C., & Wakelam, V. 2012, MNRAS, 426, 354
de Barros, A. L. F., Mejía, C., Seperuelo Duarte, E., et al. 2022, MNRAS, 511, 2491
el Akel, M., Kristensen, L. E., Le Gal, R., et al. 2022, A&A, 659, A100
Esplugues, G. B., Tercero, B., Cernicharo, J., et al. 2013, A&A, 556, A143
Esplugues, G. B., Viti, S., Goicoechea, J. R., et al. 2014, A&A, 567, A95
Esplugues, G., Fuente, A., Navarro-Almaida, D., et al. 2022, A&A, 662, A52
Esplugues, G., Rodríguez-Baras, M., San Andrés, D., et al. 2023, A&A, 678, A199
Frerking, M. A., Linke, R. A., & Thaddeus, P. 1979, ApJ, 234, L143
Frerking, M. A., Langer, W. D., & Wilson, R. W. 1982, ApJ, 262, 590
Fontani, F., Roueff, E., Colzi, L., et al. 2023, A&A, 680, A58
Garozzo, M., Fulvio, D., Kanuchova, Z., et al. 2010, A&A, 509, A67
Garrod, R. T., & Herbst, E. 2006, A&A, 457, 927
Goldsmith, P. F., & Linke, R. A. 1980, ApJ, 81, 30064
Goldsmith, P. F., & Langer, W. D. 1999, ApJ, 517, 209
Gronowski, M., & Kołos, R. 2014, ApJ, 792, 89
Gottlieb, C. A., Gottlieb, E. W., Litvak, M. M., et al. 1978, ApJ, 219, 77
Gudeman, C. S., Haese, N. N., Piltch, N. D., et al. 1981, ApJ, 246, L47
Hatchell, J., Thompson, M. A., Millar, T. J., et al. 1998, A&A, 338, 713
Herbst, E., & Klemperer, W. 1973, ApJ, 185, 505
Inostroza-Pino, N., Palmer, C. Z., Lee, T. J., et al. 2020, J. Mol. Spectrosc., 369, 111273
Jenkins, E. B. 2009, ApJ, 700, 1299
Jiménez-Escobar, A., & Muñoz Caro, G. M. 2011, A&A, 536, A91
Kalenskii, S. V., Slysh, V. I., & Val'tts, I. E. 2002, Astron. Rep., 46, 96
Kalenskii, S. V., Kaiser, R. I., Bergman, P., et al. 2022, ApJ, 932, 5
Li, J., Wang, J., Zhu, Q., et al. 2015, ApJ, 802, 40
Li, Y., Wang, J., Li, J., et al. 2022, MNRAS, 512, 4934
Lis, D. C., Goldsmith, P. F., Güsten, R., et al. 2023, A&A, 669, L15
Luo, G., Feng, S., Li, D., et al. 2019, ApJ, 885, 82
Martin-Pintado, J., Bachiller, R., & Fuente, A. 1992, A&A, 254, 315
McClure, M. K., Rocha, W. R. M., Pontoppidan, K. M., et al. 2023, Nat. Astron., 7, 431
Miessler, G. L., Fischer, P. J., & Tarr, D. A. 2013, Inorganic Chemistry, 5th edn., (london: Pearson)
Minh, Y. C., Ziurys, L. M., Irvine, W. M., et al. 1991, ApJ, 366, 192
Montaigne, H., Geppert, W. D., Semaniak, J., et al. 2005, ApJ, 631, 653
Müller, H. S. P., Thorwirth, S., Roth, D. A., et al. 2001, A&A, 370, L49
Müller, H. S. P., Schlöder, F., Stutzki, J., et al. 2005, J. Mol. Struc., 742, 215
Navarro-Almaida, D., Le Gal, R., Fuente, A., et al. 2020, A&A, 637, A39
Narita, K., Sakamoto, S., Koda, J., et al. 2024, ApJ, 969, 102
Neufeld, D. A., Godard, B., Gerin, M., et al. 2015, A&A, 577, A49
Panessa, M., Seifried, D., Walch, S., et al. 2023, MNRAS, 523, 6138
Potapov, A., Krasnokutski, S. A., Jäger, C., et al. 2021, ApJ, 920, 111
Reid, M. J., Menten, K. M., Brunthaler, A., et al. 2014, ApJ, 783, 130
Reid, M. J., Pesce, D. W., & Riess, A. G. 2019, ApJ, 886, L27
Ruaud, M., Wakelam, V., & Hersant, F. 2016, MNRAS, 459, 3756
Santos, J. C., Linnartz, H., & Chuang, K.-J. 2023, A&A, 678, A112
Schilke, P., Walmsley, C. M., Pineau des Forets, G., et al. 1997, A&A, 321, 293
Schwartz, P. R., Zuckerman, B., & Bologna, J. M. 1982, ApJ, 256, L55
Shingledecker, C. N., Lamberts, T., Laas, J. C., et al. 2020, ApJ, 888, 52
Thaddeus, P., Kutner, M. L., Penzias, A. A., et al. 1972, ApJ, 176, L73
Turner, B. E. 1989, ApJS, 70, 539
Tychoniec, Ł., van Dishoeck, E. F., van't Hoff, M. L. R., et al. 2021, A&A, 655, A65
Ulich, B. L., & Haas, R. W. 1976, ApJS, 30, 247
van der Tak, F. F. S., Black, J. H., Schöier, F. L., et al. 2007, A&A, 468, 627
van Dishoeck, E. F., Kristensen, L. E., Mottram, J. C., et al. 2021, A&A, 648, A24
Vidal, T. H. G., & Wakelam, V. 2018, MNRAS, 474, 5575
Vidal, T. H. G., Loison, J.-C., Jaziri, A. Y., et al. 2017, MNRAS, 469, 435
Wakelam, V., Castets, A., Ceccarelli, C., et al. 2004, A&A, 413, 609
Yan, Y. T., Henkel, C., Kobayashi, C., et al. 2023, A&A, 670, A98
Zhang, X., Quan, D., Li, R., et al. 2023, MNRAS, 521, 1578

Appendix A: Spectra for individual sources

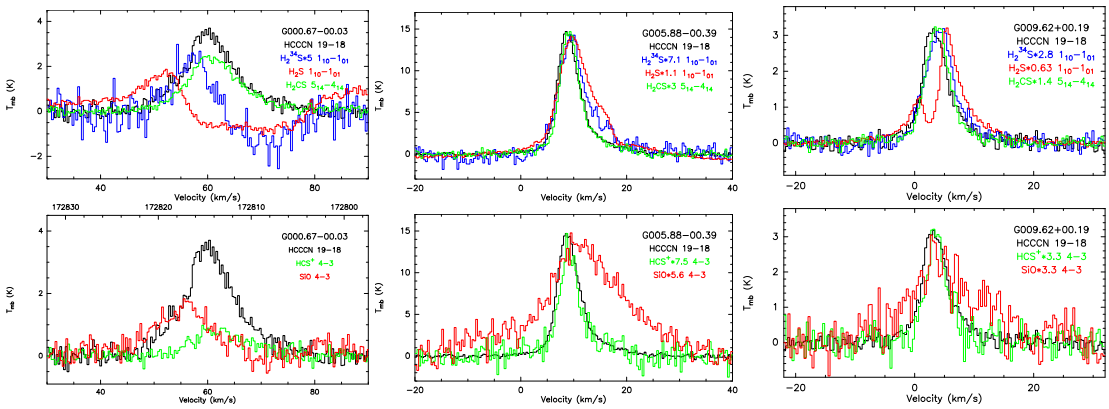

Fig. A.1: Same as Figure 1 but for more sources. Additional figures are available on Zenodo.https://doi.org/10.5281/zenodo.13937627

Appendix B: Beam-averaged column densities

Table B.1: Beam-averaged column densities.

Source	[b]N(H_2S) 10^{14} cm^{-2}	[c]N(H_2S) 10^{14} cm^{-2}	N($H_2{}^{34}S$) 10^{13} cm^{-2}	N(H_2CS) 10^{13} cm^{-2}	N(HCS^+) 10^{12} cm^{-2}	N(HC_3N) 10^{14} cm^{-2}	N(SiO) 10^{12} cm^{-2}	N($C^{18}O$) 10^{16} cm^{-2}	N(H_2) 10^{22} cm^{-2}
G000.67-00.03	[a]39.7±0.9	7.31±0.65	4.39±0.39	55.3±0.20	34.8±1.9	10.7 ± 0.17	62.8±1.1	11.0±0.04	48.0±0.18
G005.88-00.39	29.1±0.2	22.9±0.41	11.2±0.20	39.5±0.61	29.2±1.1	20.4 ± 0.26	92.5±1.4	3.76±0.02	16.4±0.09
G009.62+00.19	[a]17.7±0.1	12.3±0.31	6.49±0.16	20.8±0.27	14.6±0.6	4.47 ± 0.09	26.0±1.0	4.77±0.01	20.8±0.05
G010.47+00.02	[a]45.4±0.3	26.5±0.42	15.0±0.24	65.3±0.28	60.4±1.8	11.8 ± 0.07	31.0±0.74	3.91±0.02	17.1±0.08
G010.62-00.38	[a]49.6±0.2	35.0±0.31	18.3±0.16	62.1±0.14	49.9±0.7	10.0 ± 0.09	34.9±0.52	9.37±0.01	40.9±0.06
G011.49-01.48	1.11±0.02	0.36±0.16	0.17±0.07	2.43±0.23	2.55±0.62	0.87 ± 0.07	≤1.07	0.62±0.01	2.72±0.05
G011.91-00.61	[a]4.72±0.20	3.54±0.14	1.75±0.07	5.88±0.14	3.72±0.24	1.40 ± 0.03	8.19±0.24	1.27±0.01	5.55±0.04
G012.80-00.20	[a]8.44±0.03	6.50±0.12	3.17±0.06	21.4±0.13	20.6±0.2	4.77 ± 0.02	7.50±0.15	7.30±0.01	31.9±0.03
G012.88+00.48	[a]10.1±0.08	7.05±0.10	3.39±0.05	14.5±0.11	10.7±0.2	1.85 ± 0.08	8.39±0.18	3.54±0.01	15.4±0.03
G012.90-00.26	[a]8.34±0.07	6.38±0.15	3.07±0.07	10.8±0.15	6.31±0.32	2.40 ± 0.04	9.61±0.34	3.86±0.01	16.9±0.05
G014.33-00.64	[a]8.29±0.13	6.80±0.33	3.12±0.15	21.6±0.37	14.4±0.7	3.00 ± 0.10	29.4±1.4	1.32±0.01	5.75±0.04
G015.03-00.67	[a]2.54±0.02	2.15±0.20	1.01±0.09	2.72±0.09	2.42±0.26	2.05 ± 0.03	≤0.48	0.86±0.01	3.77±0.03
G016.58-00.05	[a]5.58±0.05	4.15±0.13	2.06±0.06	8.96±0.11	5.84±0.23	1.25 ± 0.03	8.27±0.30	2.67±0.01	11.6±0.03
G023.00-00.41	[a]4.94±0.06	3.61±0.13	1.83±0.06	4.82±0.11	3.08±0.27	1.32 ± 0.03	5.92±0.23	3.39±0.01	14.8±0.04
G023.44-00.18	2.98±0.05	2.15±0.08	1.12±0.04	6.39±0.12	4.59±0.22	0.74 ± 0.03	9.51±0.23	4.31±0.01	18.8±0.06
G027.36-00.16	8.09±0.06	5.86±0.11	3.03±0.05	16.6±0.15	7.94±0.25	2.35 ± 0.04	18.7±0.33	2.32±0.01	10.2±0.03
G028.86+00.06	6.44±0.05	4.60±0.09	2.37±0.05	7.34±0.09	6.05±0.16	1.08 ± 0.02	3.05±0.16	2.73±0.01	11.9±0.03
G029.95-00.01	21.8±0.1	16.0±0.25	8.07±0.12	19.4±0.24	13.6±0.6	3.85 ± 0.10	15.1±0.67	3.51±0.01	15.3±0.04
G031.28+00.06	[a]5.67±0.12	4.04±0.19	1.00±0.09	13.6±0.17	9.98±0.44	1.40 ± 0.05	6.76±0.45	2.65±0.01	11.6±0.04
G031.58+00.07	[a]4.72±0.05	3.50±0.16	1.74±0.08	9.12±0.15	5.19±0.24	0.97 ± 0.03	6.76±0.22	2.37±0.01	10.3±0.04
G032.04+00.05	[a]7.16±0.05	5.33±0.12	2.66±0.06	10.9±0.11	8.35±0.29	1.67 ± 0.03	16.1±0.23	2.21±0.01	9.65±0.03
G034.39+00.22	0.98±0.01	0.83±0.06	0.38±0.03	2.23±0.06	1.30±0.10	0.27 ± 0.01	3.78±0.12	1.62±0.01	7.08±0.02
G035.02+00.34	[a]6.27±0.03	5.01±0.10	2.36±0.05	8.33±0.08	7.16±0.17	1.76 ± 0.02	5.47±0.19	1.59±0.01	6.96±0.03
G035.19-00.74	[a]6.17±0.04	5.06±0.22	2.37±0.10	13.2±0.13	8.57±0.32	2.73 ± 0.03	5.78±0.20	1.97±0.01	8.59±0.05
G035.20-01.73	4.24±0.02	3.37±0.14	1.62±0.07	4.22±0.09	3.65±0.17	0.35 ± 0.03	2.69±0.23	1.05±0.01	4.58±0.02
G037.43+01.51	1.89±0.01	1.62±0.07	0.75±0.03	4.27±0.09	3.19±0.17	0.62 ± 0.02	3.54±0.15	1.44±0.01	6.28±0.02
G043.16+00.01	[a]18.3±0.09	15.5±0.22	7.04±0.10	25.3±0.17	23.9±0.5	7.10 ± 0.06	37.6±0.36	5.67±0.01	24.8±0.04
G043.79-00.12	[a]5.42±0.03	4.28±0.15	2.07±0.07	10.0±0.11	8.99±0.25	1.14 ± 0.03	8.57±0.20	2.23±0.01	9.74±0.04
G049.48-00.36	16.3±0.09	13.3±0.19	6.28±0.09	26.9±0.06	11.4±0.5	8.16 ± 0.04	27.1±0.52	3.64±0.02	15.9±0.08
G049.48-00.38	[a]43.2±0.1	33.2±0.25	15.8±0.12	125±0.16	58.2±1.0	15.3 ± 0.09	64.3±1.5	6.89±0.03	30.1±0.11
G059.78+00.06	3.09±0.02	2.60±0.07	1.18±0.03	6.00±0.07	5.65±0.17	0.63 ± 0.02	0.93±0.14	0.74±0.01	3.25±0.02
G069.54-00.97	[a]2.79±0.02	2.40±0.12	1.08±0.05	5.45±0.08	4.04±0.15	1.45 ± 0.02	4.83±0.17	1.79±0.01	7.83±0.02
G075.76+00.33	[a]3.84±0.01	3.44±0.11	1.53±0.05	6.91±0.05	5.34±0.14	1.04 ± 0.01	2.01±0.10	0.91±0.01	3.97±0.03
G078.12+03.63	1.67±0.01	1.51±0.10	0.67±0.05	3.92±0.12	2.89±0.23	1.66 ± 0.03	9.88±0.44	0.63±0.01	2.74±0.02
G081.75+00.59	1.85±0.03	1.63±0.06	0.72±0.03	3.70±0.05	3.24±0.13	0.78 ± 0.01	2.71±0.17	1.71±0.01	7.48±0.02
G081.87+00.78	7.59±0.04	6.72±0.12	2.99±0.05	17.5±0.12	10.3±0.3	4.19 ± 0.03	23.7±0.32	2.61±0.01	11.4±0.04
G092.67+03.07	2.93±0.02	2.60±0.07	1.15±0.03	10.3±0.07	7.22±0.13	1.43 ± 0.02	15.5±0.21	0.66±0.01	2.89±0.02
G109.87+02.11	[a]3.39±0.01	3.09±0.13	1.36±0.06	3.03±0.06	2.38±0.18	2.34 ± 0.03	8.56±0.28	2.36±0.01	10.3±0.02
G111.54+00.77	[a]4.42±0.03	4.13±0.06	1.76±0.02	7.13±0.05	5.47±0.10	0.81 ± 0.01	4.96±0.10	1.48±0.01	6.45±0.02
G121.29+00.65	[a]1.54±0.01	1.41±0.06	0.62±0.03	3.85±0.03	3.28±0.07	0.50 ± 0.01	2.34±0.08	0.87±0.01	3.80±0.01
G123.06-06.30	2.13±0.01	2.01±0.04	0.84±0.02	7.98±0.04	5.93±0.09	0.73 ± 0.01	10.4±0.11	0.72±0.01	3.16±0.02
G133.94+01.06	[a]9.99±0.04	8.85±0.15	3.74±0.06	22.5±0.12	17.8±0.2	2.66 ± 0.02	15.6±0.16	1.86±0.01	8.12±0.03
G168.06+00.82	[a]0.64±0.03	0.72±0.25	0.26±0.08	0.71±0.09	0.67±0.22	0.17 ± 0.07	≤0.47	0.33±0.01	1.45±0.03
G176.51+00.20	[a]0.78±0.01	0.73±0.09	0.31±0.04	1.45±0.05	1.19±0.12	0.20 ± 0.01	1.16±0.13	0.56±0.01	2.44±0.01
G183.72-03.66	0.52±0.01	0.50±0.04	0.21±0.02	1.52±0.04	1.41±0.09	0.21 ± 0.01	2.81±1.12	0.26±0.01	1.13±0.01
G188.94+00.88	1.87±0.01	1.82±0.09	0.75±0.04	4.11±0.07	3.86±0.15	0.26 ± 0.01	2.02±0.10	0.58±0.01	2.53±0.02
G192.60-00.04	3.81±0.01	3.60±0.07	1.52±0.03	4.53±0.07	4.95±0.15	0.46 ± 0.02	3.97±0.18	0.96±0.01	4.18±0.02
G209.00-19.38	1.78±0.01	1.63±0.05	0.72±0.02	1.94±0.32	2.03±0.08	0.47 ± 0.01	3.53±0.13	0.40±0.01	1.76±0.01
G232.62+00.99	0.93±0.01	0.88±0.07	0.38±0.03	2.30±0.05	2.90±0.21	0.49 ± 0.02	≤0.33	0.63±0.01	2.75±0.02
G211.59+01.05	0.82±0.01	0.82±0.03	0.33±0.01	1.34±0.03	1.35±0.07	0.15 ± 0.01	2.06±0.07	0.47±0.01	2.06±0.01

Notes. [a] The flux of H_2S lines were obtained using the "print are" method. [b] The beam-averaged column densities of H_2S were calculated using corrected optical depths. [c] The beam-averaged column densities of H_2S were derived from those of $H_2{}^{34}S$ using $^{32}S/^{34}S$ ratios.

Appendix C: The line widths at half maximum of the molecules.

Table C.1: Line widths at half maximum of the molecules in km s^{-1}.

Source	HC_3N	$H_2{}^{34}S$	H_2CS	HCS^+	SiO
G000.67-00.03	12.0 ± 0.24	11.3 ± 0.81	12.28 ± 0.25	12.7 ± 0.78	13.0 ± 0.30
G005.88-00.39	5.23 ± 0.08	6.38 ± 0.14	4.62 ± 0.09	4.86 ± 0.24	27.5 ± 0.55
G009.62+00.19	5.34 ± 0.14	5.98 ± 0.15	4.94 ± 0.08	4.34 ± 0.22	26.5 ± 1.47
G010.47+00.02	9.64 ± 0.06	6.46 ± 0.43	8.37 ± 0.06	7.06 ± 0.64	14.9 ± 0.56
G010.62-00.38	7.49 ± 0.08	6.57 ± 0.07	7.03 ± 0.04	7.13 ± 0.12	9.96 ± 0.19
G011.49-01.48	1.93 ± 0.15	0.66 ± 0.39	2.40 ± 0.25	2.50 ± 0.51	undetected
G011.91-00.61	6.71 ± 0.15	6.51 ± 0.29	5.68 ± 0.17	4.64 ± 0.40	13.1 ± 0.52
G012.80-00.20	5.38 ± 0.03	5.57 ± 0.12	5.22 ± 0.02	5.38 ± 0.07	7.09 ± 0.18
G012.88+00.48	4.11 ± 0.19	4.14 ± 0.06	3.71 ± 0.03	3.34 ± 0.07	11.9 ± 0.34
G012.90-00.26	4.77 ± 0.10	4.71 ± 0.12	4.51 ± 0.08	4.09 ± 0.25	11.8 ± 0.55
G014.33-00.64	3.26 ± 0.14	3.00 ± 0.12	2.98 ± 0.09	2.83 ± 0.17	18.4 ± 1.03
G015.03-00.67	2.63 ± 0.04	3.85 ± 0.32	2.37 ± 0.12	2.25 ± 0.29	undetected
G016.58-00.05	4.69 ± 0.15	3.82 ± 0.11	4.06 ± 0.05	3.53 ± 0.16	9.62 ± 0.49
G023.00-00.41	6.32 ± 0.22	8.14 ± 0.34	4.99 ± 0.25	5.71 ± 0.62	17.2 ± 0.87
G023.44-00.18	4.16 ± 0.20	3.76 ± 0.19	4.24 ± 0.10	4.27 ± 0.26	14.7 ± 0.45
G027.36-00.16	7.46 ± 0.19	6.28 ± 0.14	5.43 ± 0.06	4.78 ± 0.18	13.0 ± 0.33
G028.86+00.06	4.28 ± 0.11	4.21 ± 0.11	3.39 ± 0.05	2.98 ± 0.10	7.11 ± 0.54
G029.95-00.01	6.25 ± 0.21	4.67 ± 0.09	3.95 ± 0.06	3.69 ± 0.20	10.8 ± 0.67
G031.28+00.06	3.75 ± 0.16	3.93 ± 0.17	3.98 ± 0.06	3.25 ± 0.17	7.36 ± 0.64
G031.58+00.07	3.36 ± 0.11	3.73 ± 0.16	3.39 ± 0.06	3.08 ± 0.17	7.09 ± 0.28
G032.04+00.05	5.79 ± 0.13	6.24 ± 0.16	5.32 ± 0.07	5.23 ± 0.22	12.2 ± 0.22
G034.39+00.22	2.95 ± 0.21	3.29 ± 0.32	3.00 ± 0.11	1.86 ± 0.14	4.37 ± 0.19
G035.02+00.34	5.87 ± 0.06	4.58 ± 0.08	4.47 ± 0.05	4.14 ± 0.12	9.56 ± 0.48
G035.19-00.74	4.73 ± 0.07	5.08 ± 0.16	4.58 ± 0.06	3.86 ± 0.17	8.63 ± 0.44
G035.20-01.73	3.48 ± 0.62	3.73 ± 0.11	2.96 ± 0.08	2.93 ± 0.25	11.1 ± 1.50
G037.43+01.51	2.86 ± 0.12	2.63 ± 0.14	2.89 ± 0.07	2.65 ± 0.19	4.31 ± 0.25
G043.16+00.01	14.4 ± 0.15	16.7 ± 0.24	14.5 ± 0.11	15.8 ± 0.29	14.4 ± 0.15
G043.79-00.12	5.94 ± 0.17	5.95 ± 0.17	5.48 ± 0.06	5.50 ± 0.18	8.78 ± 0.25
G049.48-00.36	6.73 ± 0.04	7.21 ± 0.12	7.89 ± 0.07	6.58 ± 0.32	11.4 ± 0.28
G049.48-00.38	9.05 ± 0.07	8.46 ± 0.09	7.30 ± 0.03	5.89 ± 0.12	10.7 ± 0.24
G059.78+00.06	2.14 ± 0.07	1.92 ± 0.07	2.03 ± 0.03	2.16 ± 0.08	4.64 ± 0.92
G069.54-00.97	4.20 ± 0.06	3.57 ± 0.13	3.39 ± 0.06	3.09 ± 0.13	5.56 ± 0.29
G075.76+00.33	3.93 ± 0.05	3.32 ± 0.07	3.53 ± 0.03	3.35 ± 0.10	5.48 ± 0.34
G078.12+03.63	4.09 ± 0.08	3.96 ± 0.32	4.93 ± 0.19	3.64 ± 0.37	29.0 ± 1.81
G081.75+00.59	2.16 ± 0.04	2.16 ± 0.10	2.07 ± 0.03	1.95 ± 0.10	10.7 ± 1.02
G081.87+00.78	5.49 ± 0.05	4.38 ± 0.09	4.43 ± 0.04	4.03 ± 0.14	7.73 ± 0.14
G092.67+03.07	3.15 ± 0.04	2.99 ± 0.11	3.46 ± 0.03	2.91 ± 0.07	19.2 ± 0.34
G109.87+02.11	4.00 ± 0.06	4.60 ± 0.17	3.38 ± 0.15	3.14 ± 0.32	14.2 ± 0.60
G111.54+00.77	4.24 ± 0.08	4.30 ± 0.08	3.89 ± 0.03	3.79 ± 0.08	6.86 ± 0.20
G121.29+00.65	2.60 ± 0.04	2.75 ± 0.07	2.59 ± 0.03	2.36 ± 0.06	3.79 ± 0.20
G123.06-06.30	3.20 ± 0.04	3.57 ± 0.09	3.64 ± 0.02	3.42 ± 0.07	7.79 ± 0.11
G133.94+01.06	4.49 ± 0.05	5.28 ± 0.09	3.93 ± 0.02	3.81 ± 0.05	6.52 ± 0.08
G168.06+00.82	4.66 ± 1.98	1.23 ± 0.21	1.34 ± 0.30	0.83 ± 0.28	undetected
G176.51+00.20	1.89 ± 0.12	2.98 ± 0.33	2.07 ± 0.10	1.60 ± 0.23	14.8 ± 1.35
G183.72-03.66	1.95 ± 0.08	2.47 ± 0.28	2.18 ± 0.07	2.38 ± 0.18	8.55 ± 0.49
G188.94+00.88	2.49 ± 0.17	3.02 ± 0.18	2.63 ± 0.05	2.95 ± 0.13	4.00 ± 0.24
G192.60-00.04	3.72 ± 0.18	3.16 ± 0.07	2.56 ± 0.05	2.03 ± 0.08	9.18 ± 0.62
G209.00-19.38	2.21 ± 0.05	3.13 ± 0.11	2.25 ± 0.04	2.35 ± 0.11	18.8 ± 0.97
G232.62+00.99	2.12 ± 0.09	2.40 ± 0.26	1.96 ± 0.05	2.91 ± 0.20	undetected
G211.59+01.05	3.06 ± 0.16	3.27 ± 0.12	3.40 ± 0.08	2.58 ± 0.28	6.87 ± 0.29

Appendix D: $^{32}S/^{34}S$ ratios, τ_{H_2S}, and abundances.

Table D.1: Information on the $^{32}S/^{34}S$ ratios, τ_{H_2S}, and abundances.

Source	$^{32}S/^{34}S$	τ_{H_2S}	Abundance			
			H_2S (10^{-9})	H_2CS (10^{-10})	HCS^+ (10^{-11})	SiO (10^{-11})
G000.67-00.03	16.65	6.60	1.52 ± 0.13	11.5 ± 0.06	7.25 ± 0.40	13.1 ± 0.24
G005.88-00.39	20.37	3.13	13.9 ± 0.26	24.0 ± 0.39	17.8 ± 0.68	56.3 ± 0.88
G009.62+00.19	18.91	5.77	5.89 ± 0.15	9.98 ± 0.13	7.02 ± 0.29	12.5 ± 0.51
G010.47+00.02	17.67	11.2	15.5 ± 0.25	38.3 ± 0.23	35.4 ± 1.07	18.2 ± 0.44
G010.62-00.38	19.13	5.46	8.55 ± 0.08	15.2 ± 0.04	12.2 ± 0.18	8.54 ± 0.13
G011.49-01.48	21.68	0.72	6.37 ± 0.25	10.6 ± 0.27	6.70 ± 0.44	14.8 ± 0.45
G011.91-00.61	20.22	5.21	2.04 ± 0.04	6.72 ± 0.04	6.46 ± 0.07	2.4 ± 0.05
G012.80-00.20	20.52	4.61	4.56 ± 0.07	9.39 ± 0.07	6.91 ± 0.12	5.43 ± 0.12
G012.88+00.48	20.81	10.4	3.79 ± 0.09	6.41 ± 0.09	3.75 ± 0.19	5.70 ± 0.20
G012.90-00.26	20.81	5.64	11.8 ± 0.59	37.5 ± 0.71	25.0 ± 1.24	51.2 ± 2.37
G014.33-00.64	21.76	4.39	3.56 ± 0.11	7.69 ± 0.10	5.01 ± 0.20	7.10 ± 0.26
G015.03-00.67	21.17	1.47	2.44 ± 0.09	3.25 ± 0.08	2.07 ± 0.18	3.99 ± 0.16
G016.58-00.05	20.15	5.44	1.14 ± 0.04	3.39 ± 0.06	2.44 ± 0.12	5.05 ± 0.12
G023.00-00.41	19.79	5.38	5.78 ± 0.10	16.4 ± 0.15	7.82 ± 0.24	18.4 ± 0.33
G023.44-00.18	19.20	4.49	3.85 ± 0.08	6.15 ± 0.07	5.06 ± 0.13	2.56 ± 0.13
G027.36-00.16	19.35	4.69	10.5 ± 0.16	12.6 ± 0.16	8.87 ± 0.39	9.86 ± 0.44
G028.86+00.06	19.42	5.68	3.49 ± 0.16	11.8 ± 0.15	8.63 ± 0.39	5.85 ± 0.39
G029.95-00.01	19.86	5.36	3.39 ± 0.16	8.83 ± 0.15	5.03 ± 0.24	6.55 ± 0.21
G031.28+00.06	20.30	7.96	5.52 ± 0.13	11.3 ± 0.12	8.65 ± 0.30	16.7 ± 0.24
G031.58+00.07	20.08	5.35	1.17 ± 0.09	3.15 ± 0.09	1.84 ± 0.14	5.34 ± 0.17
G032.04+00.05	20.00	5.05	7.19 ± 0.15	12.0 ± 0.12	10.3 ± 0.25	7.86 ± 0.27
G034.39+00.22	21.68	2.45	5.89 ± 0.26	15.3 ± 0.17	9.98 ± 0.37	6.73 ± 0.24
G035.02+00.34	21.25	4.56	7.36 ± 0.30	9.22 ± 0.19	7.99 ± 0.37	5.87 ± 0.51
G035.19-00.74	21.32	3.38	2.57 ± 0.11	6.80 ± 0.14	5.09 ± 0.28	5.64 ± 0.25
G035.20-01.73	20.81	3.72	6.26 ± 0.09	10.2 ± 0.07	9.66 ± 0.18	15.2 ± 0.15
G037.43+01.51	21.54	1.80	4.40 ± 0.16	10.3 ± 0.12	9.22 ± 0.26	8.80 ± 0.21
G043.16+00.01	22.05	3.31	8.35 ± 0.13	16.9 ± 0.09	7.15 ± 0.29	17.1 ± 0.34
G043.79-00.12	20.66	3.65	11.1 ± 0.09	41.5 ± 0.17	19.3 ± 0.34	21.4 ± 0.52
G049.48-00.36	21.10	3.12	8.00 ± 0.22	18.5 ± 0.24	17.4 ± 0.52	2.86 ± 0.42
G049.48-00.38	21.10	6.03	3.07 ± 0.15	6.96 ± 0.10	5.16 ± 0.20	6.16 ± 0.22
G059.78+00.06	21.98	3.66	8.67 ± 0.28	17.4 ± 0.17	13.4 ± 0.36	5.07 ± 0.25
G069.54-00.97	22.19	2.86	5.51 ± 0.37	14.3 ± 0.44	10.52 ± 0.85	36.0 ± 1.62
G075.76+00.33	22.49	1.64	2.18 ± 0.08	4.94 ± 0.06	4.33 ± 0.17	3.61 ± 0.22
G078.12+03.63	22.41	0.99	5.90 ± 0.11	15.3 ± 0.11	9.01 ± 0.26	20.8 ± 0.29
G081.75+00.59	22.49	2.46	8.99 ± 0.26	35.7 ± 0.32	25.0 ± 0.48	53.5 ± 0.79
G081.87+00.78	22.49	2.20	3.00 ± 0.13	2.94 ± 0.06	2.32 ± 0.17	8.32 ± 0.27
G092.67+03.07	22.71	2.57	6.41 ± 0.09	11.1 ± 0.08	8.48 ± 0.16	7.69 ± 0.16
G109.87+02.11	22.78	1.39	3.71 ± 0.16	10.1 ± 0.09	8.64 ± 0.18	6.17 ± 0.22
G111.54+00.77	23.51	1.72	6.37 ± 0.13	25.3 ± 0.18	18.8 ± 0.31	33.0 ± 0.38
G121.29+00.65	22.92	1.49	10.9 ± 0.19	27.7 ± 0.17	21.9 ± 0.25	19.2 ± 0.21
G123.06-06.30	23.87	2.02	2.99 ± 0.38	5.94 ± 0.20	4.88 ± 0.51	4.76 ± 0.52
G133.94+01.06	23.65	4.72	4.37 ± 0.36	13.4 ± 0.35	12.4 ± 0.78	24.8 ± 1.01
G168.06+00.82	28.11	1.06	7.17 ± 0.35	16.2 ± 0.29	15.2 ± 0.59	7.99 ± 0.41
G176.51+00.20	23.29	1.07	8.62 ± 0.16	10.9 ± 0.18	11.9 ± 0.37	9.50 ± 0.44
G183.72-03.66	23.80	1.40	9.29 ± 0.27	11.0 ± 1.80	11.6 ± 0.46	20.1 ± 0.76
G188.94+00.88	24.09	1.06	4.00 ± 0.14	6.52 ± 0.14	6.6 ± 0.35	9.99 ± 0.33
G192.60-00.04	23.73	1.62	1.32 ± 0.58	8.93 ± 0.86	9.38 ± 2.28	3.93 ± 0.08
G209.00-19.38	22.78	0.98	5.70 ± 0.53	7.22 ± 0.25	6.42 ± 0.68	1.27 ± 0.01
G232.62+00.99	23.36	0.53	4.99 ± 1.72	4.90 ± 0.63	4.61 ± 1.58	3.27 ± 0.06
G211.59+01.05	25.19	1.76	3.20 ± 0.25	8.35 ± 0.20	10.5 ± 0.78	1.21 ± 0.01

Notes. The abundances of H_2S were derived from those of $H_2{}^{34}S$.

Appendix E: Abundance ratios.

Table E.1: Abundance ratios of S-bearing molecules.

Source name	[H_2S/H_2CS]	[H_2S/HCS^+]	[H_2CS/HCS^+]
G000.67-00.03	1.32 ± 0.12	21.0 ± 2.18	15.9 ± 0.86
G005.88-00.39	5.80 ± 0.14	78.4 ± 3.29	13.5 ± 0.55
G009.62+00.19	5.90 ± 0.17	83.9 ± 4.06	14.2 ± 0.62
G010.47+00.02	4.06 ± 0.07	43.8 ± 1.48	10.8 ± 0.33
G010.62-00.38	5.63 ± 0.05	70.0 ± 1.20	12.4 ± 0.19
G011.49-01.48	1.48 ± 0.66	14.1 ± 7.01	9.52 ± 2.47
G011.91-00.61	6.02 ± 0.27	95.2 ± 7.20	15.8 ± 1.10
G012.80-00.20	3.03 ± 0.06	31.5 ± 0.66	10.4 ± 0.13
G012.88+00.48	4.86 ± 0.08	66.1 ± 1.51	13.6 ± 0.26
G012.90-00.26	5.91 ± 0.16	101 ± 5.68	17.1 ± 0.90
G014.33-00.64	3.15 ± 0.16	47.2 ± 3.27	15.0 ± 0.77
G015.03-00.67	7.89 ± 0.78	88.7 ± 12.5	11.2 ± 1.25
G016.58-00.05	4.63 ± 0.16	71.1 ± 3.62	15.3 ± 0.64
G023.00-00.41	7.49 ± 0.32	117 ± 11.2	15.7 ± 1.44
G023.44-00.18	3.37 ± 0.14	46.9 ± 2.90	13.9 ± 0.73
G027.36-00.16	3.53 ± 0.07	73.9 ± 2.66	20.9 ± 0.68
G028.86+00.06	6.26 ± 0.15	76.0 ± 2.51	12.1 ± 0.35
G029.95-00.01	8.28 ± 0.16	118 ± 5.46	14.2 ± 0.65
G031.28+00.06	2.97 ± 0.14	405 ± 2.62	13.6 ± 0.63
G031.58+00.07	3.84 ± 0.19	67.5 ± 4.43	17.6 ± 0.87
G032.04+00.05	4.90 ± 0.12	63.8 ± 2.63	13.0 ± 0.47
G034.39+00.22	3.72 ± 0.30	63.7 ± 6.78	17.1 ± 1.34
G035.02+00.34	6.01 ± 0.13	69.9 ± 2.21	11.6 ± 0.30
G035.19-00.74	3.84 ± 0.17	59.0 ± 3.37	15.4 ± 0.59
G035.20-01.73	7.98 ± 0.37	92.1 ± 5.72	11.6 ± 0.59
G037.43+01.51	3.79 ± 0.18	50.6 ± 3.51	13.4 ± 0.78
G043.16+00.01	6.14 ± 0.10	64.9 ± 1.53	10.6 ± 0.21
G043.79-00.12	4.27 ± 0.16	47.7 ± 2.14	11.2 ± 0.33
G049.48-00.36	4.94 ± 0.07	117 ± 5.00	23.6 ± 0.96
G049.48-00.38	2.66 ± 0.02	57.1 ± 1.07	21.5 ± 0.37
G059.78+00.06	4.33 ± 0.13	46.0 ± 1.84	10.6 ± 0.34
G069.54-00.97	4.41 ± 0.22	59.5 ± 3.68	13.5 ± 0.55
G075.76+00.33	4.98 ± 0.16	64.5 ± 2.64	12.9 ± 0.35
G078.12+03.63	3.85 ± 0.28	52.4 ± 5.50	13.6 ± 1.17
G081.75+00.59	4.41 ± 0.17	50.3 ± 2.67	11.4 ± 0.47
G081.87+00.78	3.85 ± 0.07	65.5 ± 2.23	17.0 ± 0.51
G092.67+03.07	2.52 ± 0.07	36.0 ± 1.21	14.3 ± 0.28
G109.87+02.11	10.2 ± 0.49	130 ± 11.1	12.7 ± 0.97
G111.54+00.77	5.80 ± 0.09	75.6 ± 1.76	13.0 ± 0.26
G121.29+00.65	3.67 ± 0.16	43.0 ± 2.01	11.7 ± 0.27
G123.06-06.30	2.52 ± 0.05	33.9 ± 0.85	13.5 ± 0.22
G133.94+01.06	3.94 ± 0.07	49.8 ± 1.00	12.6 ± 0.15
G168.06+00.82	10.2 ± 3.74	108 ± 52.6	10.6 ± 3.88
G176.51+00.20	5.03 ± 0.67	61.3 ± 10.1	12.2 ± 1.34
G183.72-03.66	3.27 ± 0.28	35.2 ± 3.63	10.8 ± 0.72
G188.94+00.88	4.41 ± 0.22	47.1 ± 2.87	10.7 ± 0.44
G192.60-00.04	7.94 ± 0.19	72.8 ± 2.61	9.16 ± 0.32
G209.00-19.38	8.44 ± 1.40	80.4 ± 3.87	9.53 ± 1.60
G232.62+00.99	3.83 ± 0.31	30.4 ± 3.27	7.94 ± 0.61
G211.59+01.05	6.14 ± 0.25	61.1 ± 3.87	9.95 ± 0.58